Optimisation of electron irradiation for creating spin ensembles in hexagonal boron nitride

Materials for Quantum Technology

PAPER

Optimisation of electron irradiation for creating spin ensembles in hexagonal boron nitride

Alexander J Healey[1,*], Priya Singh[1], Islay O Robertson[1], Christopher Gavin[1], Sam C Scholten[2,3], David A Broadway[1], Philipp Reineck[1], Hiroshi Abe[4], Takeshi Ohshima[4,5], Mehran Kianinia[6,7], Igor Aharonovich[6,7] and Jean-Philippe Tetienne[1,*]

[1] School of Science, RMIT University, Melbourne VIC 3001, Australia
[2] School of Physics, University of Melbourne, Melbourne VIC 3010, Australia
[3] Centre for Quantum Computation and Communication Technology, School of Physics, University of Melbourne, Melbourne VIC 3010, Australia
[4] National Institutes for Quantum Science and Technology (QST), 1233 Watanuki, Takasaki, Gunma 370-1292, Japan
[5] Department of Materials Science, Tohoku University, 6-6-02 Aramaki-Aza, Aoba-ku, Sendai 980-8579, Japan
[6] School of Mathematical and Physical Sciences, University of Technology Sydney, Ultimo NSW 2007, Australia
[7] ARC Centre of Excellence for Transformative Meta-Optical Systems, University of Technology Sydney, Ultimo NSW 2007, Australia
* Authors to whom any correspondence should be addressed.

E-mail: alexander.healey2@rmit.edu.au and Jean-philippe.tetienne@rmit.edu.au

Keywords: quantum sensing, hbn, relaxometry, electron irradiation, spin defects, odmr, optimization

OPEN ACCESS

RECEIVED
19 April 2024

REVISED
4 June 2024

ACCEPTED FOR PUBLICATION
19 July 2024

PUBLISHED
29 July 2024

Abstract

Boron vacancy centre (V_B^-) ensembles in hexagonal boron nitride (hBN) have attracted recent interest for their potential as two-dimensional solid-state quantum sensors. Irradiation is necessary for V_B^- creation, however, to date only limited attention has been given to optimising the defect production process, especially in the case of bulk irradiation with high-energy particles, which offers scalability through the potential for creating ensembles in large volumes of material. Here we systematically investigate the effect of electron irradiation by varying the dose delivered to a range of hBN samples, which differ in their purity, and search for an optimum in measurement sensitivity. We find that moderate electron irradiation doses ($\approx 5 \times 10^{18}$ cm^{-2}) appear to offer the best sensitivity, and also observe a dependence on the initial crystal purity. These results pave the way for the scalable and cost-effective production of hBN quantum sensors, and provide insight into the mechanisms limiting V_B^- spin properties.

1. Introduction

The advent of optically active spin defects in hBN, in particular the negatively-charged boron vacancy centre (V_B^-) [1–3], has sparked excitement as van der Waals quantum sensors have opened up the possibility of moving towards atomic proximity with a target and for seamless integration with devices based on van der Waals heterostructures [4, 5]. Implementations based on single crystal flakes exfoliated from high-quality bulk crystals [6–8] and commercially-available nanopowders [9, 10] have been demonstrated, with proposed applications in fields ranging from condensed matter physics to biology [5]. Essential to the furtherance of hBN-based quantum sensing is arriving at reliable and scalable methods for creating high quality spin ensembles.

Low-energy (<100 keV) ion implantation has been a popular method for creating V_B^- ensembles so far, partly because it creates a predictable and constrained sensing layer [11]. However, this depth confinement is also a weakness since a single implantation run only activates an effectively 2D layer. Conversely, electron irradiation, at MeV energies, creates vacancies evenly throughout an irradiated volume that can extend to the millimetre scale [12]. Electron irradiation, therefore, is naturally well-suited to addressing the scalability problem by allowing the creation of V_B^- ensembles throughout entire bulk crystals or a large volume of nanoflakes. In principle, a localised (2D) layer can also still be realised by exfoliating a sufficiently thin flake from a bulk crystal [13]. Additionally, electron irradiation is accessible as a commercial service, in contrast to neutron irradiation, which has also been employed for this purpose [1, 14].

In this work, we irradiate hBN samples of varying purity with 2 MeV electrons over a range of doses between 2×10^{16} and 2×10^{19} cm^{-2}. This study design allows us to systematically examine the effect of lattice damage (proportional to irradiation dose) as well as initial crystal purity on V_B^- spin properties and measurement sensitivity.

Previous works considering V_B^- creation have focussed primarily on high-density ion implantation [11] and neutron irradiation [1], and have not explicitly investigated measurement sensitivity, which is an experiment-dependent quantity that generally scales in nontrivial ways with defect density in similar solid-state systems [15]. Furthermore, the dependence on hBN purity has also not been investigated so far. Given the dominance of the dense nuclear spin bath present in hBN in setting the spin coherence of V_B^- defects [16], it is not *a priori* clear whether defects related to irradiation damage or crystal impurities should have a strong effect on ensemble spin properties and hence measurement sensitivity.

Here we focus on the lower defect density regime (vacancy densities up to around 100 ppm), produced by electron irradiation of doses ranging from 2×10^{16} to 2×10^{19} cm^{-2}, and attempt to observe an optimum with respect to two prominent measurement modalities, ODMR and T_1 relaxometry. We find the defect density generated by a dose of 5×10^{18} cm^{-2} is optimal for a high purity micropowder, but that the trends appear different for other samples, suggesting a dependence on the existing crystal purity. These results suggest that the lower defect densities produced by this level of electron irradiation may produce more sensitive spin ensembles than the high-dose ion implantation most commonly considered in the literature so far (which can approach anticipated levels of vacancy creation nearing 1% [6]).

2. Methods

2.1. Sample preparation

A range of hBN samples were subjected to 2 MeV electron irradiation at various doses, as depicted schematically in figure 1(a). As in previous, lower-dose studies [17], the irradiation was performed under ambient conditions using a Cockcroft–Walton 2 MV 60 kW electron accelerator. The hBN samples were wrapped in aluminium foil and mounted on a water cooled copper plate.

Micropowders of two purities which we refer to as high (3–4 μm particle size, 99.99% purity from SkySpring Nanomaterials) and low purity (5 μm particle size, 98% purity from Graphene Supermarket) respectively (see optical image figure 1(b)), were selected to probe the effect of other contamination as well as irradiation on spin properties. Large particle sizes, effectively reflecting the bulk regime, were chosen to isolate these factors from surface effects [13]. We also irradiated high purity, bulk crystals (Grade A from HQ Graphene, pictured in figure 1(c)) and exfoliated individual flakes (sub-μm thickness) to demonstrate that the technique is applicable to applications that require custom sensors with large lateral size. With the exception of T_1 measurements, the results reported are from the bulk crystals to maintain a consistent collection volume with the micropowder samples, however we did also find that the spin properties of exfoliated flakes appear to be in line with those of the parent crystal.

2.2. PL collection and analysis

In principle, these samples differ only in their purity, and by subjecting them to identical electron irradiation procedures we may expect a similar density of V_B^- defects to be produced. To assess the levels of V_B^- creation, we collected photoluminescence (PL) spectra using an Ocean Insight Maya2000 Pro spectrometer, using typical illumination conditions for widefield V_B^- sensing (532 nm, peak power density ≈4.5 kW cm^{-2}). In figure 1(d) we plot PL spectra obtained for representative samples from each category, irradiated with a dose of 5×10^{18} cm^{-2}. We can see that the near-infrared fluorescence associated with the V_B^- defect (with a characteristic phonon side band (PSB) peaking at ≈800 nm) is indeed of similar amplitude in each case, but that PL exhibited below 700 nm (which we refer to as 'visible' emission henceforth) is highly variable. This visible fluorescence is attributed to a class of emitters [10, 18, 19] which, although their precise nature is unknown, are believed to be related to carbon impurities [20]. We leave investigations into optimised creation of these defects for future work, although visible PL was observed to increase with irradiation dose [17].

Although we do not consider the spin properties of these visible defects in this work, it can be seen that the tail of the visible PSB overlaps with the V_B^- emission and hence will reduce readout contrast. By filtering our PL collection (750 nm long pass filter), we are able to mostly isolate the V_B^- signal, however the variable tail of visible defect emission will add some variability to, for example, the measured PL contrast in optically detected magnetic resonance (ODMR) measurements. For our PL measurements of the micropowders we use films produced by dispersing the powder in isopropanol, dropcasting, and allowing the isopropanol to evaporate [10]. This procedure results in a relatively uniform film (see PL image in figure 1(e), where the

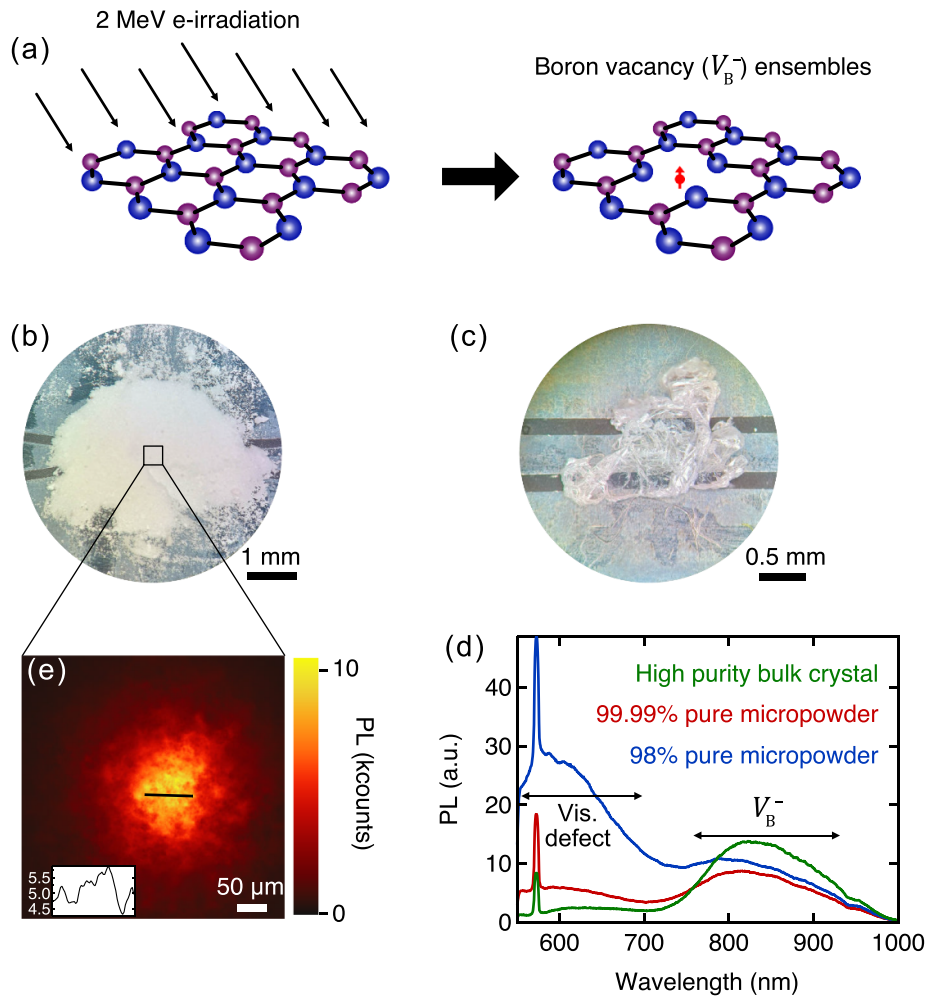

Figure 1. (a) Schematic of the electron irradiation process, resulting in the creation of V_B^- (red spin) defects in hBN. (b) hBN micropowder deposited on a microwave (MW) stripline for measurement. (c) Bulk hBN crystal on a MW stripline for measurement. (d) PL spectra taken under CW 532 nm illumination for three samples of differing initial purity following an identical electron irradiation procedure (2 MeV, 5×10^{18} cm^{-2}). The approximate PL bands belonging to 'visible' defects and near-infrared emission from V_B^- defects are marked. A similar level of V_B^- fluorescence is evident in each case but the initial purity of the crystal is linked to the level of <700 nm fluorescence. (e) Widefield V_B^- PL image of an irradiated hBN micropowder. The PL received is roughly uniform across the centre of the laser spot, shown by the inset linecut.

Gaussian shape is from the laser spot) that can be made much thicker than the expected extent of our laser spot, and hence all samples are effectively infinite in extent.

For determining shot-noise-limited sensitivity, it is more appropriate to use the PL collection rate as would be captured in a practical experiment. For our setup (introduced below), this is the count rate as measured by a scientific complementary metal oxide semiconductor (sCMOS) camera with a collection window >750 nm.

2.3. Spin measurements

Spin measurements were taken on a purpose-built room temperature widefield microscopy setup. A 532 nm laser (Quantum Opus) provides spin initialisation and readout, gated by an acousto-optic modulator (Gooch & Housego R35085-5). PL is collected through a microscope air objective (Nikon 20x S Plan Fluor ELWD, NA = 0.45) and onto an sCMOS camera (Andor Zyla). RF radiation to manipulate the spin states is supplied by a Windfreak SynthNV PRO signal generator and amplified (Mini-Circuits HPA-50 W-63+). Camera exposures, laser pulses, and RF pulses are all sequenced using a SpinCore Pulseblaster ESR 500 MHz card.

For spin measurements, hBN powders were deposited on a silver stripline (0.4 mm) dry. Pulsed ODMR sequences utilised a constant π time of 40 ns (12.5 MHz) and 500 ns laser pulses. CW ODMR sequences used a reduced Rabi frequency of 5 MHz. T_1 sequences used laser pulse durations of 1 μs.

For all spin measurements we utilised an input laser power of ≈350 mW, focussed to a spot size of ≈70 μm diameter, for a peak laser power density of ≈4.5 kW cm^{-2}.

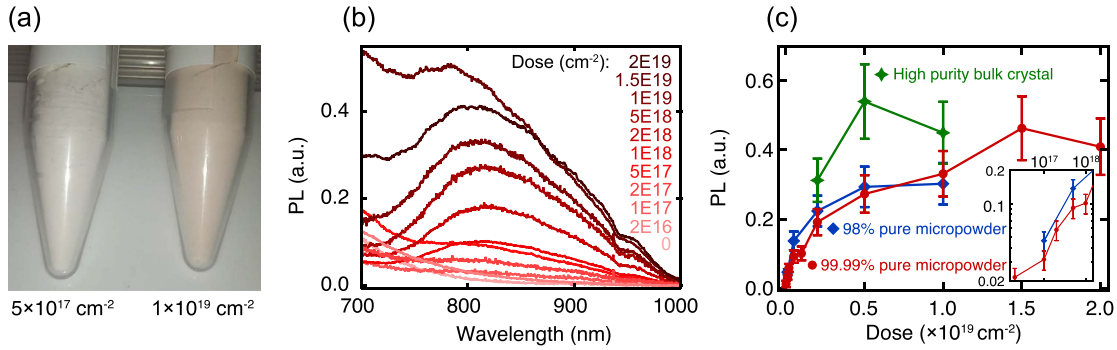

Figure 2. (a) Photograph of two vials of hBN micropowder irradiated with different 2 MeV electron doses. The higher dose (right) has a noticeably red tint. (b) PL spectra recorded under CW 532 nm laser illumination for the high purity micropowder series. The characteristic V_B^- PSB peaking around 850 nm is visible for all irradiated samples, with a variable tail from visible defect emission also evident. (c) V_B^- PL extracted from PL spectra, taking values at a constant wavelength of 830 nm. Data is presented for a lower purity (98%) micropowder and a high purity bulk crystal (HQ Graphene) as well as the samples shown in (b). The error bars are set to 20% of the values to reflect observed variation across ensembles of the order of the maximum pixel-to-pixel variation seen in the linecut in figure 1(e), which was similar to the variation in PL spectrum intensity measured at different spots. Inset is a log/log plot of the PL for doses of 1×10^{18} cm^{-2} and less.

3. Results

3.1. V_B^- photoluminescence

We begin by assessing the scaling of V_B^- PL signal with electron irradiation dose. The as-received samples do not exhibit any V_B^- fluorescence, and become fluorescent above 750 nm following irradiation. For the powdered samples, the high levels of defect creation following high doses are accompanied by an increased red tint, as shown in figure 2(a). In figure 2(b) we show the PL spectra (focussing on the V_B^- emission band now) for one set of samples, the high purity micropowder, which we irradiated with the widest range of doses. The lowest dose (2×10^{16} cm^{-2}) is successful in activating a V_B^- ensemble, with the PL increasing with higher doses.

We summarise the PL signal observed for all samples in figure 2(c), where we plot the peak V_B^- PL at ~830 nm for simplicity. At this wavelength, the influence of the visible PL tail is largely suppressed and so the trends plotted are attributed solely to the V_B^- defect, however we note that the visible PL tail is more significant for the lower purity micropowder.

The initial, roughly linear, increase in V_B^- PL with irradiation dose slows past roughly 2×10^{18} cm^{-2}, indicating we approach saturation (figure 2(c)). Assuming we predominantly create single vacancies (which is expected for these irradiation doses), the sub-linear scaling at higher doses may indicate that the proportion of boron vacancies that are negatively charged decreases with increasing dose, in line with recent observations made in the high-defect density regime [21]. The high purity bulk crystal exhibits higher PL than the powders which may be due to the higher quality material offering a more favourable Fermi level position for V_B^- formation. However, we also cannot discount an optical contribution; the powder deposition (see figure 1(b)) likely results in more scattering which could impact laser delivery and PL collection.

We do not have a direct measurement of vacancy creation in our samples, however, Murzakhanov *et al* [22] estimated a V_B^- density of 5.7 ppm via an electron paramagnetic resonance (EPR) measurement, created by 2 MeV electron irradiation at a dose of 6×10^{18} cm^{-2} in a bulk hBN crystal. This is in broad agreement with the expectation based on previous empirical and Monte Carlo studies into electron irradiation of materials such as diamond [12] and recent quantification of relevant energy scales in hBN [23], the combination of which suggests that a 2 MeV electron should produce order 1×10^{-4} vac./μm on average. This V_B^- density is comparable to the value reported following neutron irradiation in Gottscholl *et al* [3] (also measured by EPR), and is an order of magnitude lower than the densities estimated in Gong *et al* [21] for He^+ irradiation. In this context, the range of irradiation doses considered in our work is expected to range from among the lowest defect creation densities considered so far in the literature for ensemble V_B^- creation, well below 1 ppm, to those achievable by low-dose ion implantation (above 100 ppm vacancy production).

3.2. ODMR properties and DC sensitivity

Ultimately, we are primarily concerned with the sensitivity of a spin-based measurement, which absolute PL will be but one factor in. Other spin properties will play into the measurement sensitivity, which we characterise on a typical widefield sensing apparatus. Two measurement modalities have mainly been used in V_B^--based sensing so far, ODMR and T_1 relaxometry, which we will consider in turn.

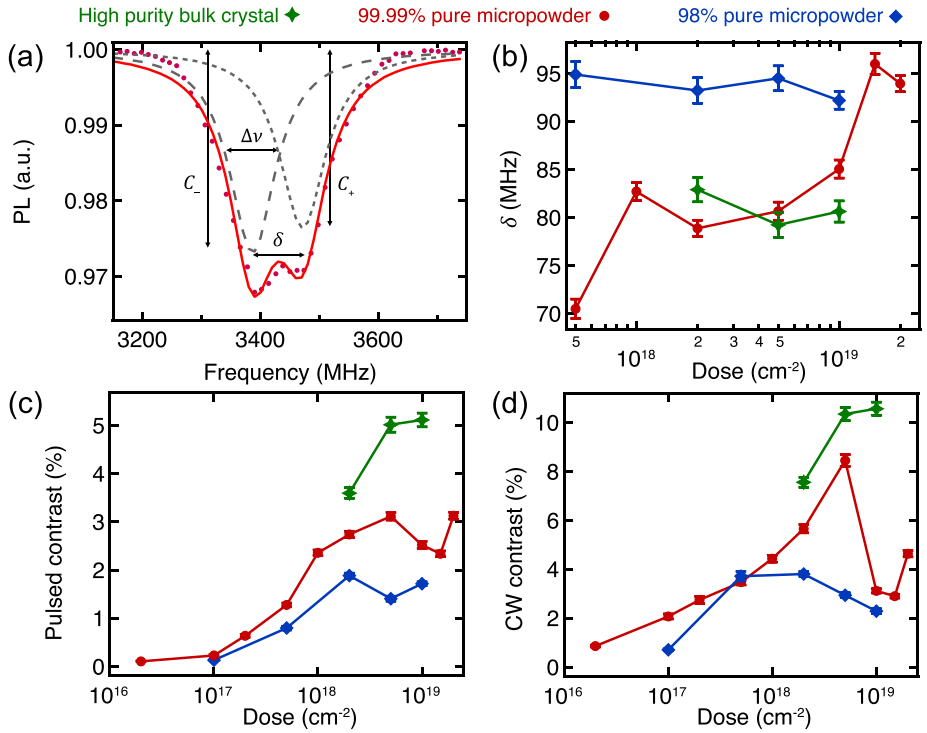

Figure 3. (a) Pulsed ODMR spectrum taken at zero magnetic field (high-purity micropowder, irradiation dose 1×10^{19} cm^{-2}). The dots are the experimental data and the solid red line is a fit based on the sum of two Lorentzian lineshapes (grey dashed traces). These Lorentizans are centred at frequencies f_- and f_+, have amplitudes C_- and C_+ and a shared full width at half maximum (FHWM) $\Delta\nu$. (b) The splitting between f_+ and f_-, δ, which is related to the electric field E. δ is related to the charged defect density and is accordingly seen to increase with irradiation dose. A correlation with the initial crystal purity is also evident. The extraction of ODMR splitting for samples irradiated with less than 5×10^{17} was unreliable and so we do not include these measurements. (c) Pulsed ODMR contrast versus irradiation dose. The trends between samples are very different, indicating a strong dependence on initial crystal purity. The contrast plotted here is the average of the two fit amplitudes C_- and C_+. (d) CW ODMR contrast. All error bars represent the standard errors from the curve fitting. We note that non-V_B^- visible background PL was observed to be variable in time and so the fit error may not fully account for the variability in contrast in our samples.

In figure 3(a) we show a typical pulsed ODMR spectrum under zero magnetic field, for a high purity micropowder sample following a dose of 1×10^{19} cm^{-2}. ODMR spectra such as this can be fit using two Lorentzian lineshapes with a shared width $\Delta\nu$ and individual amplitudes (contrasts $\mathcal{C}_-$ and $\mathcal{C}_+$) and central frequencies (f_- and f_+), where the prescription $\pm$ refers to the resonance belonging to the transition between the two spin transitions within the ground state. The resonance contrasts and linewidths are relevant in determining measurement sensitivity (as we will see below) and the resonance locations can be linked to the quantities $D = (f_+ + f_-)/2$, the zero-field splitting parameter, and $\delta = (f_+ - f_-)$, which may be expected to scale with irradiation dose as they can be related to lattice strain and charged defect density respectively [21, 24]. As well as pulsed ODMR, wherein the excitation/readout laser is temporally separated from the microwave (MW) drive, it is also possible to conduct continuous wave (CW) ODMR, where laser and MW are applied simultaneously. Despite incurring additional power broadening [25], CW ODMR often results in higher sensitivity measurements for V_B^- sensing, however can also produce sharp increases in temperature that can be undesirable [6]. In the following, we will consider both pulsed and CW protocols for extracting sensitivities and restrict ourselves to pulsed ODMR for the extraction of the zero-field resonant frequencies.

We start by looking at the δ parameter in figure 3(b). There is a clear increasing trend evident for the high-purity micropowder series, for which doses over nearly two orders of magnitude are considered, while the trend is less stark in the other two series. This quantity has previously been related to a charged defect concentration in the higher density regime with the proportionality $\delta \propto 2d_\perp E_\perp$ [21, 26], where $E_\perp$ is the transverse electric field and $d_\perp \approx 35$ Hz/V.cm^{-1} is the V_B^- transverse electric field susceptibility [21]. Comparing to Gong *et al* [21], the values of δ corresponding to the highest doses studied are consistent with charged defect densities approaching 100 ppm, as expected. In the ideal case, the number of charged defects present in the crystal would be twice the V_B^- density (half belonging to the V_B^- defects and half to the counterpart positively-charged electron donors), however it is also possible that the irradiation produces other charged defects, for instance charged vacancies on nitrogen sites and more complex defects. The larger δ values measured for the lower-purity micropowder corroborate this expectation, likely being due to a higher pre-existing charged defect density, including that related to the strong visible emission observed in

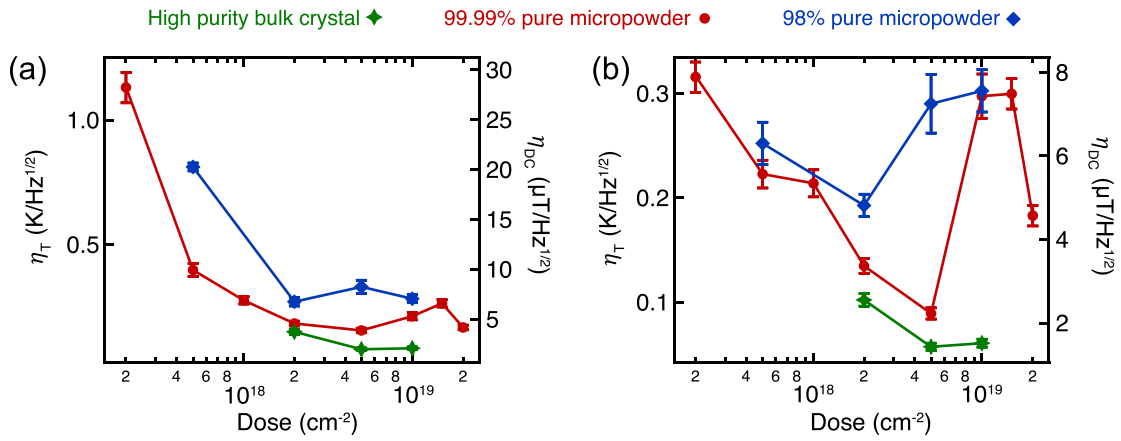

Figure 4. (a) Temperature (left axis) and DC magnetic field (right) sensitivity calculated for the different samples, based on pulsed ODMR measurements. Here we consider PL collected from a ≈70 × 70 μm^2 region under 350 mW laser excitation, collecting all PL above 750 nm. (b) As (a) but using CW ODMR measurements. Note we exclude data from doses lower than 2×10^{17} cm^{-2} for plot readability.

figure 1(d). Previous measurements have estimated the paramagnetic defect density of similar hBN powders at above 10 ppm [10], which matches the current data.

Moving to ODMR contrast, we see some evidence for differing trends versus irradiation dose based on the purity of the starting material. Starting with a high power pulsed (40 ns π pulse) protocol in figure 3(c), we see that, similar to the PL data, the high-purity micropowder series features a peak in contrast at 5×10^{18} cm^{-2}, while the lower purity powder's contrast peaks at 2×10^{18} cm^{-2} and the bulk crystal exhibits a higher contrast that does not appear to fully saturate versus irradiation dose up to 1×10^{19} cm^{-2}. The difference between the three series [which we note is separate to the PL trends in figure 2(c)] may be due to an increase in PL from other defects or a reduction in spin pumping arising from a charge migration effect in the higher defect density regime [27, 28].

In figure 3(d) we plot the CW ODMR contrast, which features similar trends with a crucial difference: a more sudden drop in contrast after 5×10^{18} cm^{-2} for the high-purity micropowder, accompanied by a steady drop versus dose in the low-purity powder. The cause of the exacerbation of the trends observed in the pulsed ODMR case is unclear, but may support the interpretation that complicated charge dynamics during laser illumination are relevant. We also note that the low-purity micropowder, with its more significant visible PL and electric field splitting, exhibits the lowest PL contrast and tends to decrease with dose from a maximum at 2×10^{18} cm^{-2}, especially in the CW series, while the high purity bulk crystal contrast increases monotonically with irradiation dose over the range considered. One possible interpretation is that impurities present may form defects following irradiation that alter V_B^- charge cycling behaviours [27, 28] and add background PL that partially overlaps with V_B^-. However, more work is required to confirm the mechanism behind the effect observed.

To benchmark the quality of the ensembles produced for ODMR-based sensing, we consider the sensitivity to temperature shifts at zero field, which is given by [29]

$$\eta_T = \frac{4}{3\sqrt{3}} \frac{2\pi}{\alpha} \frac{\Delta\nu}{\mathcal{C}\sqrt{\mathcal{R}}}, \tag{1}$$

where $\alpha = 0.70$ MHz/K is the V_B^- temperature coefficient when linearising the response near room temperature [3, 6, 30], $\Delta\nu$ is the power broadened ODMR linewidth, $\mathcal{C}$ is the ODMR contrast, and $\mathcal{R}$ is the photon count rate, which is effectively equal to the value under CW laser illumination given the high duty cycle in even our pulsed measurements. Note that we focus on temperature sensitivity here since we mainly consider ensembles of powders that feature randomly-oriented defects on average and hence are not suited to measuring magnetic fields, however the DC magnetic field sensitivity can be obtained by multiplying equation (1) by α/γ_e, where γ_e is the electron gyromagnetic ratio. This quantity is displayed on the right axes of figure 4, however this is indicative only since away from zero field the hyperfine structure of the V_B^- defect will broaden its ODMR resonance more significantly, leading to a greater linewidth [6].

The results are plotted in figure 4, where we separate the sensitivity extracted using pulsed (figure 4(a)) and CW (figure 4(b)) ODMR. The sensitivity values reported are based on PL collection from illuminated regions approximately 70 μm in diameter, using a 20×, NA = 0.45 objective. The trends are similar in both cases (mostly following the trends in contrast as this quantity was the most variable), with optimal

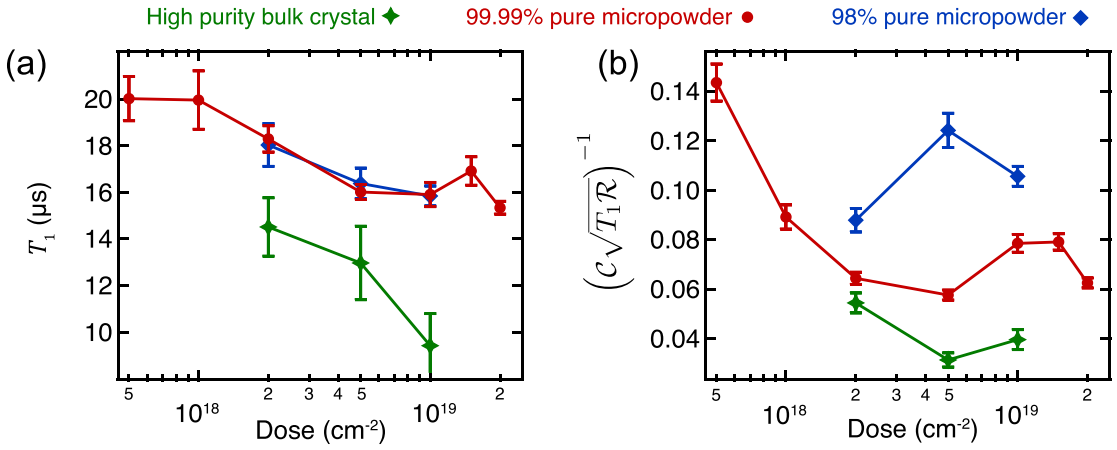

Figure 5. (a) T_1 values recorded versus irradiation dose. T_1 decreases with irradiation dose, likely due to the introduction of magnetic noise and possibly due to modification of phonons. No dependence on the initial crystal purity is evident. (b) figure of merit proportional to sensitivity (inverse to SNR) of a relaxometry measurement. The difference between the two powders is primarily due to the measurement contrast since T_1 and the PL count rate are similar between the two series. An optimal sensitivity is again found for a dose of 5×10^{18} cm^{-2} in the case of the high purity micropowder and bulk crystal.

sensitivities obtained with a dose of 5×10^{18} cm^{-2} in the case of the higher purity crystals, and the lower dose of 2×10^{18} cm^{-2} for the lower purity powder. The sensitivities obtained using pulsed and CW protocols in this case are similar at the optimal doses, with the CW protocol performing better on average, although we note that the pulsed protocol can avoid laser heating of a sample and so will likely be preferred in practice.

3.3. T_1 and relaxometry sensitivity

Finally, we measure the spin relaxation time T_1, which sets the practical upper limit for spin coherence and the sensitivity of relaxometry experiments [9, 31]. Here we use longer laser pulse durations, ≈1 μs (up from 500 ns), to ensure high, uniform initialisation into the $|0\rangle$ ground state across the ensemble [9]. The results are plotted in figure 5(a), and we find a consistent dependence on irradiation dose across the various data sets. The reduction we observe for the micropowders, down to about 15 μs for a dose of 2×10^{19} cm^{-3}, is again consistent with previous ion implantation results [21, 32], again assuming that our level of defect creation is at the 100 ppm level and below. This result implies that additional damage introduced by the irradiation is a relatively minor source of accelerated spin relaxation compared to the processes that limit room temperature T_1 to ≈20 μs, and there is no apparent dependence on crystal purity. Given the importance of high initialisation for accurate T_1 measurements, we measure individual flakes exfoliated from the bulk crystal, rather than the parent crystal as before.

The mechanism behind the temperature scaling of V_B^- T_1 is still an open question, but could include phonon and thermally-activated magnetic noise components [33]. Given that the T_1 trends appear to be insensitive to the pre-existing charged defect density [c.f. figure 3(b)], one possible inference could be that the irradiation process modifies the phonon spectrum through the lattice damage introduced [34]. The T_1 values recorded for flakes exfoliated from bulk crystals are consistently lower than the micropowders, although they are typical of exfoliated flakes measured elsewhere in the literature [13]. One interpretation in our case could be that the smaller hBN particles heat up during irradiation and effectively anneal, so that the vacancy density produced in the bulk crystals is actually higher. This conclusion may be supported by the higher levels of PL and spin contrast observed in the bulk crystals compared to micropowders with the same irradiation dose, however this is only a speculative conclusion at this stage.

Again assuming a shot-noise-limited measurement, the sensitivity of a T_1 relaxometry measurement will be proportional to [9]

$$\eta_{T_1} \sim \left(\mathcal{C}\sqrt{T_1\mathcal{R}}\right)^{-1}, \tag{2}$$

where $\mathcal{C}$ is the contrast of the T_1 measurement, proportional to the pulsed ODMR contrast. Note that this is a unitless quantity and that the sensitivity of a T_1 relaxometry measurement will also be dependent on the distance between sensor and target, as well as the properties of the magnetic noise being sensed [31]. This figure of merit is plotted in figure 5(b), where we find similar scaling and hierarchy as in figure 4. An irradiation dose of 5×10^{18} cm^{-2} appears optimal, except for the low-purity micropowder due to the trends in spin contrast—overall the trend in T_1 are too subtle to overcome the more significant variation in contrast

between the samples. Note we use the same PL values as before for the 'high purity bulk crystal' data so that the comparison between data series is fair.

4. Conclusion

In this work we have found that electron irradiation is effective in activating V_B^- ensembles over a wide range of doses. Since electron irradiation carries the major advantage of scalability over ion implantation (which is depth-confined) and accessibility compared to neutron irradiation, we expect that the technique will be particularly useful for creating large amounts of quantum-active hBN nano and micropowders, and bulk crystals to facilitate repeated exfoliation of single crystal flakes for incorporation into van der Waals heterostructures.

We find that a dose of 5×10^{18} cm^{-2} appears optimal for high purity crystals on our setup, while lower doses may be preferred for lower-quality starting material. If the defect density created by this dose is optimal regardless of the creation method, our results could imply that greater sensitivities can be obtained by considering lower density ensembles than have been prioritised in the literature so far, such as through high-dose ion implantation. More work is required to determine which impurities determine the scaling in V_B^- creation versus irradiation dose and through what mechanism, however it is likely that the position of the Fermi level both during irradiation and measurement plays a role.

The dependence of sensitivity on initial crystal purity is strongly linked to background fluorescence from visible emitters that are present in a higher quantity in the lower purity powders. The most significant difference comes from a degradation in readout contrast, which is likely due to a combination of background fluorescence overlapping our PL collection window and an increased abundance of nearby defect sites that promote non-radiative decay pathways during illumination. The limiting ODMR linewidths and spin relaxation times, are not strongly linked to the hBN purity, being governed primarily by the dense nuclear spin bath and mechanical properties of the crystal respectively. We do, however, corroborate previous studies that found a dependence of these properties on irradiation-induced lattice damage, confirming that this damage is significant even at the low end of defect creation. Future work could consider whether other treatments such as annealing under moderate temperatures [35] can produce more sensitive V_B^- ensembles and whether the optimal irradiation dose is changed.

Data availability statement

The data that support the findings of this study are available from corresponding authors upon reasonable request.

Acknowledgments

The authors thank Brett Johnson for fruitful discussions. This work was supported by the Australian Research Council (ARC) through Grants CE200100010, FT200100073, FT220100053, DE200100279, DP220100178, DP220102518, and DE230100192, and by the Office of Naval Research Global (N62909-22-1-2028). P R acknowledges support through an Australian Research Council DECRA Fellowship (Grant No. DE200100279) and an RMIT University Vice-Chancellor's Senior Research Fellowship. I O R is supported by an Australian Government Research Training Program Scholarship. S C S gratefully acknowledges the support of an Ernst and Grace Matthaei scholarship. Part of this study was supported by QST President's Strategic Grant 'QST International Research Initiative'.

ORCID iDs

Alexander J Healey https://orcid.org/0000-0001-5727-0288
Islay O Robertson https://orcid.org/0000-0001-6477-517X
Sam C Scholten https://orcid.org/0000-0001-8494-9341
Takeshi Ohshima https://orcid.org/0000-0002-7850-3164
Mehran Kianinia https://orcid.org/0000-0003-4073-1492
Igor Aharonovich https://orcid.org/0000-0003-4304-3935
Jean-Philippe Tetienne https://orcid.org/0000-0001-5796-2508

References

[1] Gottscholl A *et al* 2020 Initialization and read-out of intrinsic spin defects in a van der Waals crystal at room temperature *Nat. Mater.* **19** 540–5
[2] Gottscholl A, Diez M, Soltamov V, Kasper C, Sperlich A, Kianinia M, Bradac C, Aharonovich I and Dyakonov V 2021 Room temperature coherent control of spin defects in hexagonal boron nitride *Sci. Adv.* **7** eabf3630
[3] Gottscholl A, Diez M, Soltamov V, Kasper C, Krauße D, Sperlich A, Kianinia M, Bradac C, Aharonovich I and Dyakonov V 2021 Spin defects in hBN as promising temperature, pressure and magnetic field quantum sensors *Nat. Commun.* **12** 4480
[4] Aharonovich I, Tetienne J-P and Toth M 2022 Quantum emitters in hexagonal boron nitride *Nano Lett.* **22** 9227–35
[5] Vaidya S, Gao X, Dikshit S, Aharonovich I and Li T 2023 Quantum sensing and imaging with spin defects in hexagonal boron nitride *Adv. Phys.* X **8** 1
[6] Healey A J *et al* 2023 Quantum microscopy with van der Waals heterostructures *Nat. Phys.* **19** 87–91
[7] Huang M *et al* 2022 Wide field imaging of van der Waals ferromagnet Fe 3 GeTe 2 by spin defects in hexagonal boron nitride *Nat. Commun.* **13** 5369
[8] Kumar P *et al* 2022 Magnetic imaging with spin defects in hexagonal boron nitride *Phys. Rev. Appl.* **18** 061002
[9] Robertson I O *et al* 2023 Detection of paramagnetic spins with an ultrathin van der Waals quantum sensor *ACS Nano* **17** 13407–17
[10] Scholten S C et al, Multi-species optically addressable spin defects in a van der Waals material (2023) (arXiv: 2306.16600v1)
[11] Kianinia M, White S, Fro J E, Bradac C and Aharonovich I 2020 Generation of spin defects in hexagonal boron nitride *ACS Photon.* **7** 2147–52
[12] Campbell B, Choudhury W, Mainwood A, Newton M and Davies G 2002 Lattice damage caused by the irradiation of diamond *Nucl. Inst. Methods Phys. Res.* A **476** 680–5
[13] Durand A *et al* 2023 Optically-active spin defects in few-layer thick hexagonal boron nitride *Phys. Rev. Lett.* **131** 116902
[14] Toledo J R, Jesus D B D, Kianinia M, Leal A S, Fantini C, Cury L A, Sáfar G A M, Aharonovich I and Krambrock K 2018 Electron paramagnetic resonance signature of point defects in neutron-irradiated hexagonal boron nitride *Phys. Rev.* B **98** 155203
[15] Healey A J, Stacey A, Johnson B C, Broadway D A, Teraji T, Simpson D A, Tetienne J-P and Hollenberg L C L 2020 Comparison of different methods of nitrogen-vacancy layer formation in diamond for wide-field quantum microscopy *Phys. Rev. Mater.* **4** 104605
[16] Haykal A *et al* 2022 Decoherence of V_b- spin defects in monoisotopic hexagonal boron nitride *Nat. Commun.* **13** 4347
[17] Ngoc My Duong H, Nguyen M A P, Kianinia M, Ohshima T, Abe H, Watanabe K, Taniguchi T, Edgar J H, Aharonovich I and Toth M 2018 Effects of high-energy electron irradiation on quantum emitters in hexagonal boron nitride *ACS Appl. Mater. Interfaces* **10** 24886–91
[18] Stern H L, Gu Q, Jarman J, Barker S E, Mendelson N, Chugh D, Schott S, Tan H H, Sirringhaus H and Aharonovich I 2022 Room-temperature optically detected magnetic resonance of single defects in hexagonal boron nitride *Nat. Commun.* **13** 618
[19] Rassi E, Zhang Y, Mendoza G, Méndez J C, Merchant H and Haegens S 2023 Coherent control of an ultrabright single spin in hexagonal boron nitride at room temperature *Nat. Commun.* **14** 2923
[20] Mendelson N *et al* 2021 Identifying carbon as the source of visible single-photon emission from hexagonal boron nitride *Nat. Mater.* **20** 321–8
[21] Gong R, He G, Gao X, Ju P, Liu Z, Ye B, Henriksen E A, Li T and Zu C 2023 Coherent dynamics of strongly interacting electronic spin defects in hexagonal boron nitride *Nat. Comm.* **14** 3229
[22] Murzakhanov F F, Yavkin B V, Mamin G V, Orlinskii S B, Mumdzhi I E, Gracheva I N, Gabbasov B F, Smirnov A N, Davydov V Y and Soltamov V A 2021 Creation of negatively charged boron vacancies in hexagonal boron nitride crystal by electron irradiation and mechanism of inhomogeneous broadening of boron vacancy-related spin resonance lines *Nanomaterials* **11** 1373
[23] Bui T A, Leuthner G T, Madsen J, Monazam M R A, Chirita A I, Postl A, Mangler C, Kotakoski J and Susi T 2023 Creation of single vacancies in hBN with electron irradiation *Small* **19** 2301926
[24] Lyu X, Tan Q, Wu L, Zhang C, Zhang Z, Mu Z, Zúñiga-Pérez J, Cai H and Gao W 2022 Strain quantum sensing with spin defects in hexagonal boron nitride *Nano Lett.* **22** 6553–9
[25] Dréau A, Lesik M, Rondin L, Spinicelli P, Arcizet O, Roch J-F and Jacques V 2011 Avoiding power broadening in optically detected magnetic resonance of single NV defects for enhanced dc magnetic field sensitivity *Phys. Rev.* B **84** 195204
[26] Udvarhelyi P, Clua-Provost T, Durand A, Li J, Edgar J H, Gil B, Cassabois G, Jacques V and Gali A 2023 A planar defect spin sensor in a two-dimensional material susceptible to strain and electric fields *npj Comput. Mater.* **9** 150
[27] Manson N B, Hedges M, Barson M S J, Ahlefeldt R, Doherty M W, Abe H, Ohshima T and Sellars M J 2018 NV—N+ pair centre in 1b diamond *New J. Phys.* **20** 113037
[28] Capelli M *et al* 2022 Proximal nitrogen reduces the fluorescence quantum yield of nitrogen-vacancy centres in diamond Proximal nitrogen reduces the fluorescence quantum yield of nitrogen-vacancy centres in diamond *New J. Phys.* **24** 033053
[29] Barry J F, Schloss J M, Bauch E, Turner M J, Hart C A, Pham L M and Walsworth R L 2020 Sensitivity optimization for NV-diamond magnetometry *Rev. Mod. Phys.* **92** 15004
[30] Liu W *et al* 2021 Temperature-dependent energy-level shifts of spin defects in hexagonal boron nitride *ACS Photon.* **8** 1889–95
[31] Tetienne J-P, Hingant T, Rondin L, Cavaillès A, Mayer L, Dantelle G, Gacoin T, Wrachtrup J, Roch J F and Jacques V 2013 Spin relaxometry of single nitrogen-vacancy defects in diamond nanocrystals for magnetic noise sensing *Phys. Rev.* B **87** 235436
[32] Guo N J *et al* 2022 Generation of spin defects by ion implantation in hexagonal boron nitride *ACS Omega* **7** 2
[33] Mondal S and Lunghi A 2023 Spin-phonon decoherence in solid-state paramagnetic defects from first principles *npj Comput. Mater.* **9** 120
[34] Zhang W, Li H, Jiang H, Wu H, Lu Y, Zhao X, Liu L, Gao Y and Zhang L 2021 Influence of surface defects on the thermal conductivity of hexagonal boron nitride/poly(dimethylsiloxane) Nanocomposites: a molecular dynamics simulation *Langmuir* **37** 12038–48
[35] Suzuki T, Yamazaki Y, Taniguchi T, Watanabe K, Nishiya Y, Matsushita Y-i, Harii K, Masuyama Y, Hijikata Y and Ohshima T 2023 Spin property improvement of boron vacancy defect in hexagonal boron nitride by thermal treatment *Appl. Phys. Express* **16** 032006